JOURNAL OF GEOPHYSICAL RESEARCH, VOL. 113, D14S21, doi:10.1029/2007JD009655, 2008

Radiative susceptibility of cloudy atmospheres to droplet number perturbations: 2. Global analysis from MODIS

Lazaros Oreopoulos[1] and Steven Platnick[2]

Received 29 November 2007; revised 21 February 2008; accepted 10 April 2008; published 25 July 2008.

[1] Global distributions of albedo susceptibility for areas covered by liquid clouds are presented for 4 months in 2005. The susceptibility estimates are based on expanded definitions presented in a companion paper and include relative cloud droplet number concentration (CDNC) changes, perturbations in cloud droplet asymmetry parameter and single-scattering albedo, atmospheric/surface effects, and incorporation of the full solar spectrum. The cloud properties (optical thickness and effective radius) used as input in the susceptibility calculations come from MODIS Terra and Aqua Collection 5 gridded data. Geographical distributions of susceptibility corresponding to absolute (''absolute cloud susceptibility'') and relative (''relative cloud susceptibility'') CDNC changes are markedly different indicating that the detailed nature of the cloud microphysical perturbation is important for determining the radiative forcing associated with the first indirect aerosol effect. However, both types of susceptibility exhibit common characteristics such as significant reductions when perturbations in single-scattering properties are omitted, significant increases when atmospheric absorption and surface albedo effects are ignored, and the tendency to decrease with latitude, to be higher over ocean than over land, and to be statistically similar between the morning and afternoon MODIS overpasses. The satellite-based susceptibility analysis helps elucidate the role of present-day cloud and land surface properties in indirect aerosol forcing responses. Our realistic yet moderate CDNC perturbations yield forcings on the order of 1–2 W m^{-2} for cloud optical property distributions and land surface spectral albedos observed by MODIS. Since susceptibilities can potentially be computed from model fields, these results have practical application in assessing the reasonableness of model-generated estimates of the aerosol indirect radiative forcing.

Citation: Oreopoulos, L., and S. Platnick (2008), Radiative susceptibility of cloudy atmospheres to droplet number perturbations: 2. Global analysis from MODIS, *J. Geophys. Res.*, *113*, D14S21, doi:10.1029/2007JD009655.

1. Introduction

[2] Studies investigating the modification of cloud microphysical and optical properties by anthropogenic aerosol, commonly referred to as the Indirect Aerosol Effect (IAE) have become more numerous in recent years, in no small part because of the availability of new ground-based observational systems like the Aerosol Robotic Network (AERONET) [*Holben et al.*, 1998], as well as the development of models that attempt to account for aerosol sources and transport [e.g., *Chin et al.*, 2007]. Satellite observations have also been used to study the IAE [e.g., *Bréon et al.*, 2002; *Coakley and Walsh*, 2002; *Sekiguchi et al.*, 2003; *Kaufman et al.*, 2005; *Koren et al.*, 2005]. However, there are many challenges in isolating cloud changes due to aerosol effects alone, while all relevant dynamic/thermodynamic quantities remain fixed. These challenges include the need to identify and then quantify the background (premodified) state of the cloud, the relationship between column aerosol optical thickness and CCN concentrations at cloud level, and cloud-dependent dynamic/thermodynamic changes that correlate with changes in aerosol amounts. Rather than confronting the formidable task of assessing the partial derivative of cloud properties in a particular place and time, we have adopted an alternative approach where satellite retrievals are used to estimate the radiative response or sensitivity to some specified change in cloud droplet number concentration (CDNC) under constant liquid water content and water path conditions. While these CDNC perturbations can be due to a variety of underlying causes, our intention is to contribute to the understanding of the 1st IAE or ''Twomey effect'' (the albedo increase of constant liquid water path clouds as they become optically thicker because of more numerous, but smaller, droplets). In essence, our method is therefore an attempt to quantify the

[1] Joint Center for Earth Systems Technology, University of Maryland, Baltimore County, Baltimore, Maryland, USA.
[2] Laboratory for Atmospheres, NASA Goddard Space Flight Center, Greenbelt, Maryland, USA.

0148-0227/08/2007JD009655$09.00

climate impact of well-posed hypothetical cloud modification scenarios, and does not address previous cloud albedo modifications that may have already occurred.

[3] Global spatial and temporal distributions of the albedo sensitivity under fixed liquid water content and path conditions can be used to estimate the range of future radiative forcings due to the Twomey effect, as well as provide an additional constraint in indirect effect modeling studies. The concept of "cloud susceptibility" [*Platnick and Twomey*, 1994] provides a framework to examine this impact from theoretical, observational, and global modeling standpoints. The theoretical standpoint was the focus of a companion paper [*Platnick and Oreopoulos*, 2008, hereinafter referred to as Part 1], while the global observational standpoint is the focus of this paper. Solar flux perturbations based entirely on output from global climate models is the subject of future work taking advantage of recent advances in representing cloud droplet microphysics in such models [e.g., *Fountoukis and Nenes*, 2005; *Ming et al.*, 2006].

[4] The work presented here broadens previous satellite-based cloud susceptibility studies that were limited to narrowband cloud albedo changes in the visible part of the spectrum due to a fixed absolute increase in CDNC [*Platnick and Twomey*, 1994; *Chuang et al.*, 2002]. As explained in Part 1, in order to address broadband albedo susceptibility, including relative CDNC changes, perturbations in the cloud droplet asymmetry parameter and single-scattering albedo stemming from modified effective droplet sizes must be taken into account in addition to perturbation in cloud extinction. While the former effects are sometimes relatively small, they are often not negligible, and are typically of the same approximate magnitude as the effects of surface albedo and atmospheric molecular absorption that were also neglected in previous susceptibility studies.

[5] Since many definitions and computational details involved in susceptibility calculations have been already discussed in Part 1, here we only provide a brief overview of the radiative transfer code and cloud microphysical relationships/perturbations (section 2), in order to concentrate on the specific MODIS Level 3 implementation. Section 3 presents geographical susceptibility distributions intended to identify the most susceptible current cloud regimes, to either absolute or relative CDNC changes, and discusses the various sources and dependencies of susceptibility variability. Section 4 provides examples of global "susceptibility forcing" estimates for our two perturbation scenarios on present-day joint optical thickness–effective radius distributions inferred from MODIS. We conclude the study in section 5 with a summary and a discussion on how global studies of susceptibility can be used by modelers and the possibilities for expanded studies in the future.

2. Data Set and Methodology of Cloud Susceptibility Calculations

[6] We use Collection 5 Level 3 daily (D3) gridded ($1^\circ \times 1^\circ$) atmosphere data from MODIS Terra ($\sim$1030 local overpass time) and Aqua ($\sim$1330 local overpass time) for January, April, July, and October 2005 [*King et al.*, 2003]. These middle months of the four meteorological seasons were chosen to approximately resolve this particular year's seasonal cycle. The scientific data sets (SDSs) we used for the susceptibility calculations (explained below) are: liquid cloud mean optical thickness ($\overline{\tau}$), liquid cloud mean effective radius ($\overline{r}_e$), mean cloud fraction of liquid clouds ($\overline{A}_c$), liquid cloud joint histograms of optical thickness (τ) and effective radius (r_e), liquid cloud joint histograms of τ and cloud top temperature (T_c), and mean solar zenith angle (SZA). The joint 2-D histograms of τ and r_e are resolved in 110 bins (11 for τ and 10 for r_e), and the joint histograms of τ and T_c are resolved in 143 bins (11 for τ and 13 for T_c). Except for high latitudes where grid points can be revisited within the same day because of orbital swath overlap, the daily histograms contain information on the instantaneous spatial variability within the $1^\circ \times 1^\circ$ grid points. Susceptibilities, which are essentially albedo differences as explained below, based on calculations using the mean cloud properties are termed "PPH (Plane-Parallel Homogeneous) susceptibilities," while susceptibilities obtained from the joint $\tau - r_e$ histograms are termed "ICA (Independent Column Approximation) susceptibilities" [see *Oreopoulos et al.*, 2007]. The distinction is discussed further below.

[7] The calculations presented here were performed with the broadband solar radiation code used in GSFC Large Scale Models [*Chou et al.*, 1998; *Chou and Suarez*, 2002], with the parameterization of the band-averaged cloud single-scattering properties modified to accommodate the MODIS r_e retrieval range, as explained in Part 1. While cloud albedo susceptibility was originally defined as the cloud albedo perturbation due to a differential change in CDNC (see equation (1a) in Part 1), with the radiative transfer (RT) algorithm at hand it is calculated as the following albedo (R) difference:

$$\Delta R = \frac{\sum_i f_i F_i^{\uparrow}(\tau_i + \Delta\tau_i, \tilde{\omega}_i + \Delta\tilde{\omega}_i, g_i + \Delta g_i)}{\mu_0 F_0^{\downarrow}} - \frac{\sum_i f_i F_i^{\uparrow}(\tau_i, \tilde{\omega}_i, g_i)}{\mu_0 F_0^{\downarrow}} \tag{1}$$

where $\Delta\tau_i$, Δg_i and $\Delta\tilde{\omega}_i$ are optical thickness, asymmetry factor and single-scattering albedo perturbations due to $\Delta r_e = r_e' - r_e < 0$ perturbations arising from either absolute CDNC changes $\Delta N > 0$ ("absolute albedo susceptibility") or relative CDNC changes $\Delta N/N > 0$ ("relative albedo susceptibility"). The index i in the above equation is for one of the four wide spectral bands of the RT algorithm where effective (band-averaged) cloud optical properties are used, μ_0 is the cosine of the solar zenith angle (SZA), $F_0^{\downarrow}$ is incident solar irradiance at the top of the atmosphere (TOA), $F_i^{\uparrow}$ is the spectral flux reflected back to space at the TOA and f_i is the fractional relative contribution to $F_0^{\downarrow}$ in band i. Though not explicit, the albedo difference calculated from equation (1) generally includes surface and atmospheric molecular effects.

[8] For both relative and absolute perturbations of CDNC the perturbed effective radius r_e' is given by

$$r_e' = r_e\left(\frac{N}{N+\Delta N}\right)^{1/3} = r_e\left(\frac{1}{1+\frac{\Delta N}{N}}\right)^{1/3} \tag{2}$$

(see Part 1, equation (11)), the difference being that for absolute perturbations the values of both N and ΔN are required. CDNCs cannot be retrieved from MODIS radiances, but values can be assigned to pixels with successful liquid cloud retrievals by assuming a certain value of liquid water content (*w)* or cloud geometrical thickness, and specifying the relationship between volume radius (r_v) and r_e [*Martin et al.*, 1994]. When a value of w is assumed, N is given by:

$$N \approx \frac{3w}{4\rho_l \pi k r_e^3} \tag{3}$$

where ρ_l is the liquid water density, and the factor k relating the cubes of r_v and r_e assumes in our study the value 0.80 for marine clouds and 0.66 for continental clouds; 0.73 is used for coastal (mixed land-ocean) grid points. As in Part 1, we set w to 0.3 gm^{-3} for our default absolute susceptibility calculations (w is not involved in relative susceptibility calculations). The sensitivity to this assumption is examined later.

[9] Surface spectral (coarsely resolved into two bands above and below 0.7 μm) albedo, needed as a boundary condition in the broadband radiation calculations, comes from the identical data sources and methods used in the operational MODIS cloud retrievals [*Platnick et al.*, 2003]. The snow-free and permanent snow/ice albedo is the 5-year climatology of *Moody et al.* [2005], which uses an ecosystem-dependent temporal interpolation technique to fill missing or seasonally snow covered data in the operational MODIS Terra surface albedo product (MOD43B3). The data are provided in a 1arc minute equal angle grid with the seasonal cycle resolved in 16-day periods. Snow and ice scenes are identified with the snow/ice index from National Oceanic and Atmospheric Administration (NOAA) microwave-derived daily 0.25° Near Real-Time Ice and Snow Extent (NISE) data set. Spectral albedos for nonpermanent snow on land surfaces are taken from lookup tables populated by seasonal MOD43B3 albedos aggregated by the MODIS Terra ecosystem product (MOD12Q1). Sea ice albedo is derived from a combination of permanent snow/ice and open ocean albedo along with an estimate for the melt season transition. In all cases, we use the diffuse ("white sky") albedo for the broad 0.3–0.7 μm and 0.7–5.0 μm bands which roughly correspond to the UV-VIS and NIR bands of the *Chou et al.* [1998] model.

[10] Atmospheric profiles of temperature and water vapor are resolved into 16 layers extending from 1000 to 10 mbar and come from the National Center for Environmental Prediction (NCEP) Global Data Assimilation System (GDAS) product [*Derber et al.*, 1991]. This data set is identical to the one used in the operational MODIS retrievals. The product also provides total (column) ozone concentration. The CO_2 concentration is set at 370 ppm. The cloud is placed in the layer whose top temperature is closest to the mean cloud top temperature ($\overline{T}_c$) as derived from the joint histogram of liquid cloud τ and T_c. Since the cloud exists only in a single layer there no need for a cloud fraction overlap assumption.

[11] As mentioned above, two types of susceptibility are calculated: the standard (absolute) albedo susceptibility according to the definition in Part 1 extending *Platnick and Twomey* [1994], which is approximated as the albedo difference of cloudy atmospheric columns whose clouds contain the same liquid water path and content, but have CDNCs that differ by ΔN = 1 cm^{-3}; and the relative susceptibility which is simply the albedo difference for atmospheric columns whose clouds have CDNCs that differ by a relative amount $\Delta N/N$. The changes in the single-scattering properties $\Delta\tau_i$, Δg_i and $\Delta\tilde{\omega}_i$ are calculated internally by the model using the parameterization of single-scattering properties as a function of r_e for each spectral band (see Part 1).

[12] To obtain susceptibility for the grid point portion covered by unobscured liquid clouds, albedo calculations were performed using either a single calculation with the mean values of liquid water cloud τ and r_e, or multiple calculations using their joint histogram. The first type of calculation is a so-called "Plane-Parallel Homogeneous" (PPH) calculation that neglects grid-scale horizontal cloud variability, while the second is an "Independent Column Approximation" (ICA) type of calculation and accounts (in principle) for horizontal heterogeneity (but no horizontal photon transfer) with two caveats: (1) the daily joint histograms in MODIS data sampling do not always strictly represent only spatial variability as explained above and (2) histogram discretization makes the calculation only an approximation to the "true" ICA.

[13] For the PPH calculations, the mean optical thickness value for a given MODIS grid point pair was considered to correspond to the model's UV-VIS band (band 1). From the extinction corresponding to the given mean value of r_e for that band, the liquid water path, W, was calculated. The W, r_e pair (from which spectral optical thicknesses are calculated) and the grid point mean SZA were then used as input to the radiative transfer algorithm for the calculation of the unperturbed reflected TOA flux and albedo (second term in the RHS of equation (1)). Following the calculation of the perturbed value of effective radius r_e' according to equation (2), we obtained a new albedo, allowing again the model to operate as usual, i.e., using r_e' for new estimates of all cloud single-scattering parameters. The difference between the two albedos (equation (1)) is our approximation for susceptibility. For ICA calculations, the procedure described above has to repeated for each of the joint histogram's central τ-r_e bin values, while albedos (perturbed and unperturbed) are calculated by weighting each bin's albedo with its normalized histogram value, and summing the albedos over all bins. Albedos and susceptibilities were calculated daily for the liquid cloud portion of each grid point. Monthly averages for each grid point were obtained by taking the cloud fraction–weighted average of the daily values. Monthly zonal averages are calculated by accumulating the cloud fraction–weighted daily grid point values within each latitude zone. Global averages use as weights the zonally averaged cloud fraction and the area of the latitude zone. Note that since susceptibility is derived numerically, the behavior of radiative perturbations for arbitrary (i.e., finite) ΔNs can also be examined (even though the change in albedo is no longer equivalent to the "susceptibility" in the differential sense). This is especially relevant when ΔNs come from a cloud microphysical model which incorporates specific emission scenarios. To facilitate presentation, all susceptibility results quoted or shown

below include a multiplication factor of 1000, and thus absolute susceptibility assumes units of mm^3.

3. Global Susceptibility Results

3.1. ICA Versus PPH Calculations of Susceptibility

[14] As stressed in the previous section, the MODIS D3 (daily) data set allows us to calculate susceptibilities using either the grid point mean liquid τ and r_e (PPH calculation) or the joint histogram (ICA calculation). The latter calculation is superior in principle since it includes (most) spatial variations affecting radiative flux estimates because of the nonlinear dependence of flux on both τ and r_e [*Barker*, 2000; *Oreopoulos et al.*, 2007]. Alas, the more accurate ICA albedos require far more calculations. For a fully populated joint histogram (rarely, if ever, the case) ICA requires 110 calculations (the number of bins in the joint histogram) versus only 1 calculation per grid point for PPH. But even if, say, 50 bins are populated in the joint histogram, to obtain the monthly averaged absolute and relative susceptibility of a grid point with and without asymmetry parameter/single-scattering albedo perturbations (see section 3.3), 5×31 days $\times$ 50 bins $\sim 8 \times 10^3$ runs of the RT model are needed. To obtain the full geographical distribution of monthly susceptibility from ICA for the 4 months of our study, for both Terra and Aqua, the number of calculations rises to $\sim 3 \times 10^9$. While these ICA susceptibilities represent the core of the results presented in the study, when examining sensitivities of susceptibility to atmospheric or surface effects (section 2.2), or other dependencies (section 2.4), we resorted to the faster PPH calculations. Also, unless otherwise stated (e.g., section 2.2), all susceptibility calculations include atmospheric and surface effects.

[15] The differences between the ICA and PPH values of absolute and relative susceptibility can be understood by considering the functional form of the dominant susceptibility term that gives the extinction perturbation (Part 1, equation (6)). For absolute susceptibility it can be expressed as:

$$\Delta R \approx k \frac{4\pi\rho_l}{9w} \tau \frac{\partial R}{\partial \tau} r_e^3 \Delta N \tag{4a}$$

while for relative susceptibility it is given by:

$$\Delta R_{rel} \approx \frac{1}{3} \tau \frac{\partial R}{\partial \tau} \frac{\Delta N}{N} \tag{4b}$$

for the cloud-only case (i.e., without atmospheric and surface effects). These equations appear equivalent because of equation (3), but recall that in equation (4a) the value of w is fixed while in equation (4b) the value of the perturbation $\Delta N/N$ is fixed. Other than the different CDNC perturbation term and the different prefactors, these expressions differ only by the factor r_e^3. A simplified two-stream expression for albedo in the case of diffuse incidence

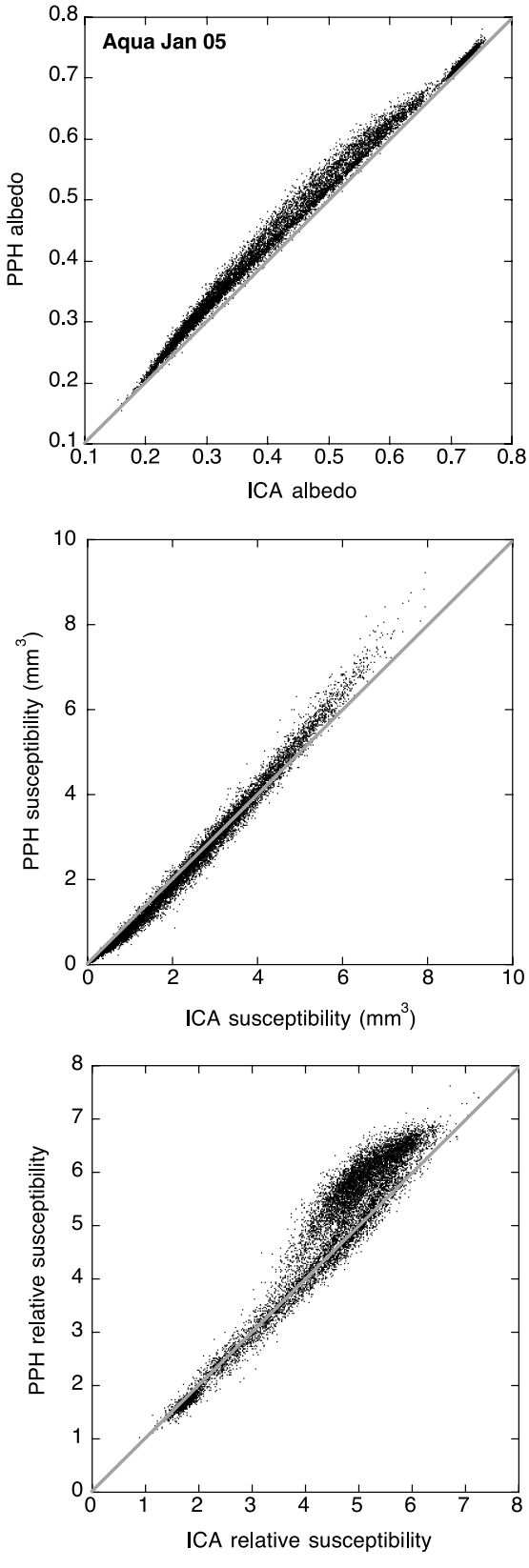

Figure 1. Relationship between monthly averaged PPH (calculated from daily grid point means) and ICA (calculated from τ-r_e joint histograms) (top) albedo, (middle) absolute susceptibility (ΔN = 1 cm^{-3}, w = 0.3 gm^{-3}), and (bottom) relative susceptibility $\times$ 1000 ($\Delta N/N$ = 10%) for MODIS Aqua January 2005 data. Every 5th grid point is plotted.

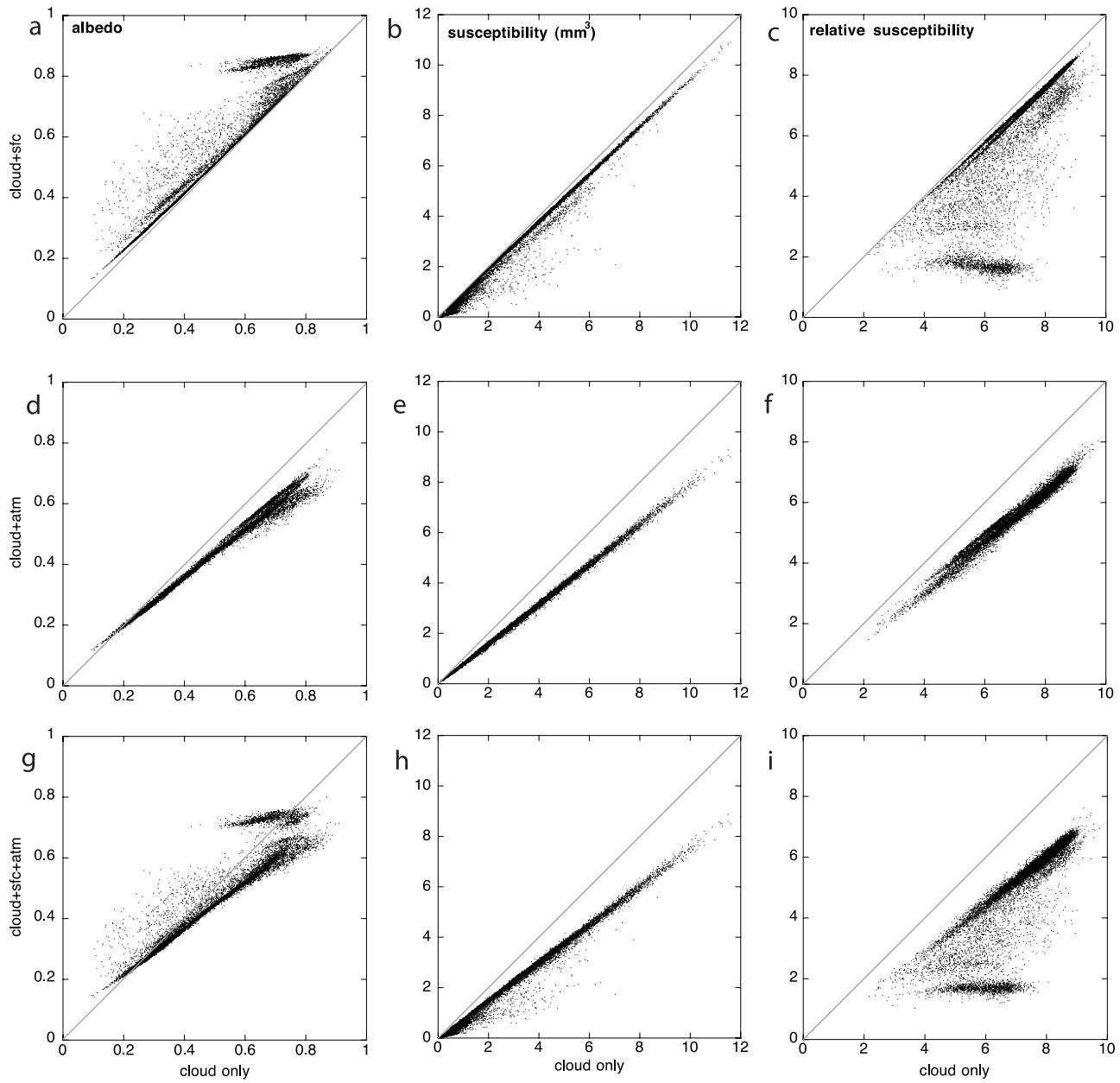

Figure 2. The impact of (a–c) surface albedo, (d–f) atmospheric effects, and (g–i) their combination on PPH albedo (Figures 2a, 2d, and 2g), absolute susceptibility ($\Delta N = 1$ cm^{-3}, $w = 0.3$ gm^{-3}) (Figures 2b, 2e, and 2h), and relative susceptibility $\times$ 1000 ($\Delta N/N = 10\%$) (Figures 2c, 2f, and 2i), as seen in scatterplots versus the corresponding cloud-only quantities. Each point is a monthly averaged grid point value for MODIS Aqua January 2005 data, and only every 5th grid point is plotted.

and conservative scattering is $R \approx [(1 - g)\tau]\ [2 + (1 - g)\tau]^{-1}$ [*Bohren*, 1987]. This yields:

$$\tau \frac{\partial R}{\partial \tau} = R(1 - R) = \frac{2(1 - g)\tau}{[2 + (1 - g)\tau]^2} \tag{5}$$

which increases to a maximum value at $\tau \approx 13$ (for $g = 0.85$) and decreases thereafter. Thus, differences between PPH and ICA relative susceptibility are driven by the nonlinearity in $\tau \frac{\partial R}{\partial \tau}$ while differences between PPH and ICA absolute susceptibility are driven by a competition between the nonlinearities in $\tau \frac{\partial R}{\partial \tau}$ and r_e^3. Of course, in the observations, the impact of nonlinearities on the PPH versus ICA calculations is ultimately determined by the extent of the τ and r_e spatial variability.

[16] Figure 1 provides an example of PPH and ICA differences from January 2005 Aqua data. Each point in the plots of Figure 1 (as in all scatterplots that follow) represents a monthly averaged 1° grid point value. Figure 1 (top) shows albedos. As expected by the convexity (with respect to optical thickness) of the albedo curve, $R_{\mathrm{PPH}} > R_{\mathrm{ICA}}$ for all grid points except a very few which find

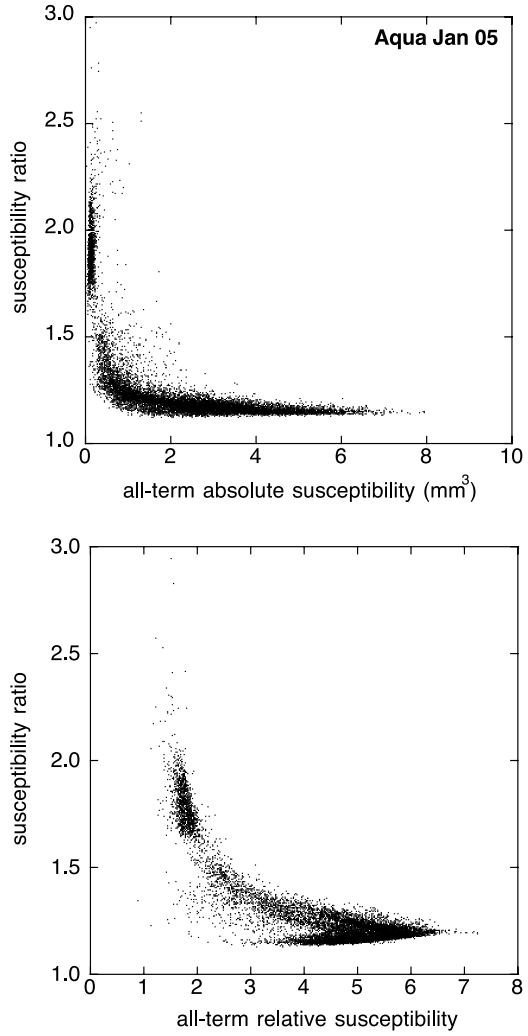

Figure 3. Ratio of all-term to one-term (i.e., with perturbations in asymmetry factor and single-scattering albedo omitted) susceptibility versus all-term susceptibility from ICA calculations. (top) Absolute susceptibility (ΔN = 1 cm^{-3}, w = 0.3 gm^{-3}) and (bottom) relative susceptibility × 1000 ($\Delta N/N$ = 10%). Data come from the monthly averaged grid point values of Aqua January 2005 calculations, and every 5th grid point is plotted.

themselves just below the one-to-one line because of errors due to the histogram discretization. Figure 1 (middle) compares ICA and PPH absolute susceptibilities (calculated for ΔN = 1 cm^{-3}, w = 0.3 gm^{-3}). ICA susceptibilities tend to be larger than PPH susceptibilities for small values of susceptibility while the opposite tends to occur for the larger values. This seems to suggest a weak spatial variability in r_e (compared to τ) controlling PPH and ICA differences despite the fact that the r_e dependence of absolute susceptibility is much stronger (see equation (4a)). Differences between PPH and ICA absolute susceptibilities are within 20% for the vast majority (~82%) of grid points. The picture is different for relative susceptibility (Figure 1 (bottom), for $\Delta N/N$ = 10%) where PPH overestimates outnumber ICA overestimates by a factor of ~2.5 and where ~87% of the grid points exhibit differences less than 20%. Relative differences are small in general because the largest absolute differences occur at high values of susceptibility. This, in turn, is probably because the maximum in $\tau \frac{\partial R}{\partial \tau}$ occurs at values of optical thickness similar to those where the albedo curve convexity is the greatest and where the PPH albedo bias is therefore also at its maximum for a given value of variability [*Cahalan et al.*, 1994]. The effective radius has negligible effect in relative susceptibility calculations because it has only a small impact on the shape of the $\tau \frac{\partial R}{\partial \tau}$ curve. For our simple closed form expression for albedo, for example, it affects this curve via its influence on g. Its effect is, of course, further diminished by the weaker spatial variability of r_e compared to τ.

3.2. Contribution From the Atmosphere and Surface

[17] One of the new elements of the present susceptibility study is the inclusion of atmospheric and surface effects in the radiative transfer calculation, which transforms cloud susceptibilities to TOA susceptibilities for atmospheric columns containing liquid clouds. Here we examine the influence on susceptibility of atmospheric and surface contributions to the TOA albedo. With the RT algorithm in our disposal we can easily switch off either the surface albedo and/or the atmospheric absorption/scattering. The results of this exercise for Aqua January data are summarized in Figure 2. Figure 2 shows how PPH albedos (Figures 2a, 2d, and 2g), absolute susceptibilities (Figures 2b, 2e, and 2h) and relative susceptibilities (Figures 2c, 2f, and 2i) with one or both of atmospheric and surface albedo effects activated compare with the counterpart quantities for the cloud alone. When a reflective surface is placed underneath the cloud in the absence of an atmosphere, the TOA albedo increases, as expected (Figure 2a). On the other hand, when an aerosol-free atmosphere is included in radiative flux calculations assuming a black surface, the TOA albedo decreases compared to that of an isolated cloud, except for small values of albedo (Figure 2d); this implies that effects due to molecular absorption dominate those due to backscattering. When both atmospheric and surface effects act simultaneously, TOA albedo is sometimes higher and sometimes lower than that of the cloud itself.

[18] The susceptibility panels of Figure 2, however, show that despite the atmospheric and surface effects having opposing influences on the TOA albedo, they both act to reduce susceptibility. The simple explanation for this behavior is that in the presence of atmospheric and surface effects, the relative contribution of a cloud to the TOA albedo is smaller than that of an isolated cloud. The reduction of susceptibility, especially in the presence of a highly reflective surface, can be quite large. This is evident in Figure 2c (relative susceptibility) where a group of points with cloud-only susceptibility ranging between about 4 × 10^{-3} to 8 × 10^{-3} has its susceptibility reduced to ~2 × 10^{-3} when a reflecting surface is included in the calculations. The above results suggest that proper accounting of the radiative sensitivity of cloud microphysics perturbations has to take into account the surrounding environment. One manifestation of this fact is that the same cloud will make an atmospheric column radiatively more susceptible when residing in a marine environment instead of a continental or polar environment.

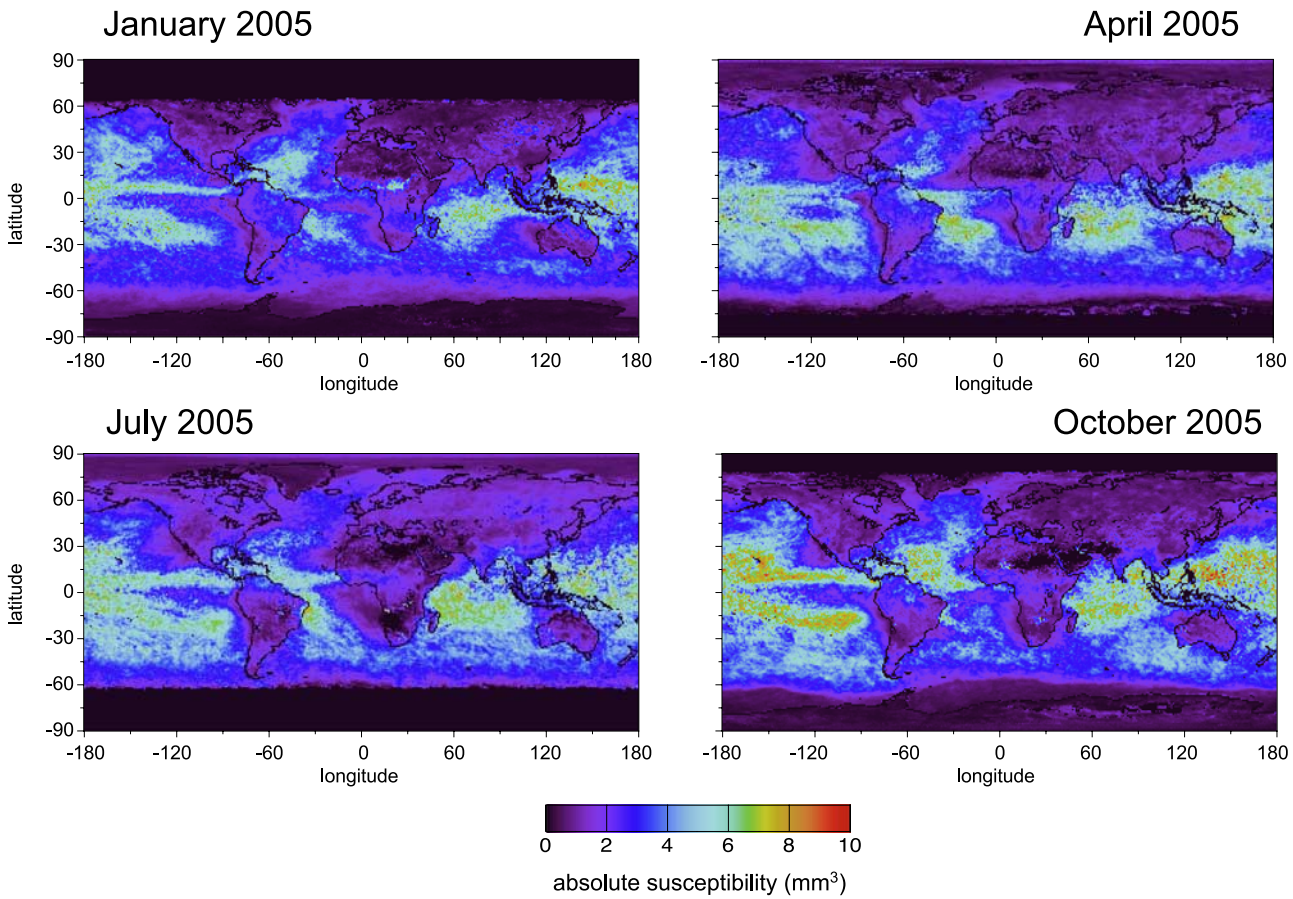

Figure 4a. Monthly averages of absolute susceptibility (ΔN = 1 cm^{-3}, w = 0.3 gm^{-3}) from MODIS Terra Level 3 τ-r_e joint histograms for January, April, July, and October 2005.

3.3. Contribution of Asymmetry Parameter and Single-Scattering Albedo Perturbations

[19] Differences between the dominant "one-term" (extinction perturbation only, equation (4)) and "all-term" (including single-scattering albedo and asymmetry parameter perturbations) susceptibilities were discussed with the aid of theoretical calculations in Part 1. Here the issue is revisited with MODIS susceptibilities incorporating spatially variable surface and atmospheric influences. Figure 3 plots the ratio of all-term to one-term susceptibility versus the all-term susceptibility for Aqua January data. The Figure 3 (top) is for absolute susceptibility while Figure 3 (bottom) is for relative susceptibility. For most grid points, the inclusion of asymmetry parameter and single-scattering perturbations contributes an additional 15–25% to the values of one-term absolute and relative susceptibility. Only for small values of susceptibility do the contributions of Δg and $\Delta\tilde{\omega}$ constitute a large fraction of the total value. A similar conclusion was drawn from the theoretical calculations of Part 1 (Figure 6, left). Hence, accurate susceptibility calculations must account for perturbations in all cloud optical properties arising from effective radius changes.

3.4. Sensitivity of Absolute Susceptibility to Liquid Water Content

[20] Our baseline absolute susceptibility calculations assume w = 0.3 gm^{-3}. An obvious question that arises is how absolute susceptibilities would change had we used a different reference value of w. Equation (4) suggests that a scaling factor of 0.3/w would be appropriate, but this would accommodate only the dominant susceptibility term which is solely due to the $\Delta\tau$ perturbation. If differences in r_e perturbations for different CDNCs arising from different assumed w's (see equation (11) in Part 1) affect Δg and $\Delta\tilde{\omega}$ perturbations only to a small extent, then all-term absolute susceptibilities for different liquid water contents are expected to be relatively well approximated by applying the scaling factor 0.3/w as well. This expectation was confirmed in a comparison between susceptibilities using our default reference value of w = 0.3 gm^{-3} and susceptibilities based on liquid water content values of 0.2 and 0.4 gm^{-3} for October 2005 PPH monthly values from Aqua. A scatterplot of absolute susceptibilities for w = 0.2 gm^{-3} and for w = 0.4 gm^{-3} against those for w = 0.3 gm^{-3} (not shown) gives regression line slopes of 1.47 and 0.76, respectively, compared to 1.50 and 0.75 predicted from 0.3/w which, as previously mentioned, is exact only when asymmetry parameter and single-scattering albedo perturbations as well as atmospheric and surface effects are neglected. This echoes theoretical results presented in Part 1 (Figure 6, middle) and suggests that absolute susceptibilities calculated for a particular value of w are easily scalable to values corresponding to a different w. We note that the size distribution parameter k, also fixed for absolute susceptibility calculations, scales in a similar

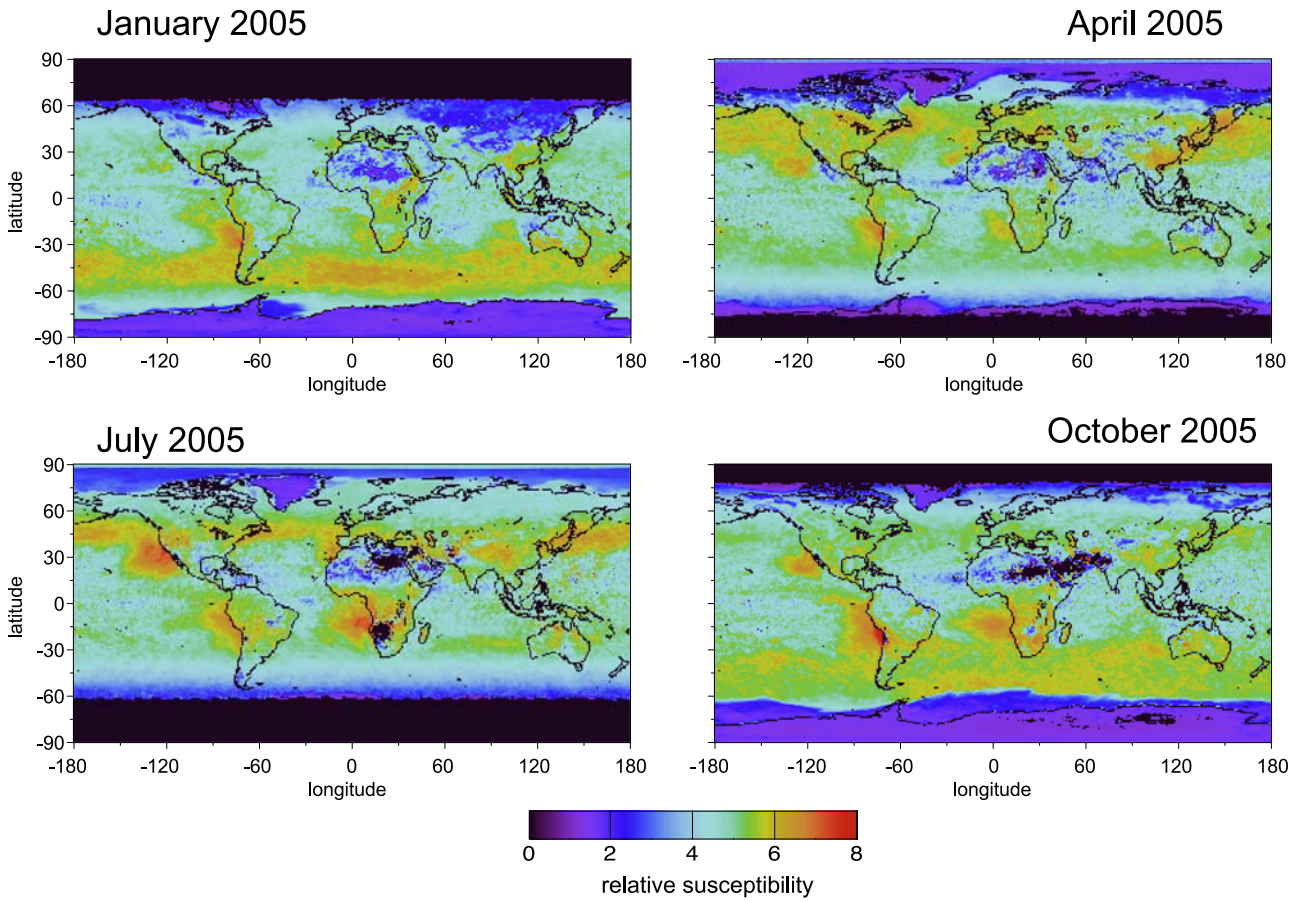

Figure 4b. As in Figure 4a but for relative susceptibility × 1000 ($\Delta N/N$ = 10%).

manner, and that albedo perturbations for relative CDNC perturbations scale well with $\Delta N/N$ (Part 1, Figure 6 (right)) even when Δg and $\Delta\tilde{\omega}$ contributions are accounted for.

3.5. Geographical Distribution of Susceptibility

[21] Figures 4a and 4b show the geographical distribution of Terra absolute and relative susceptibility, respectively, for the 4 months analyzed in this study. There are common features in all months such as the tendency for higher values of susceptibility over ocean than over land (see also Figure 7). Also, certain cloud regimes such as marine stratocumulus in regions of oceanic upwelling and marine shallow convective clouds in the equatorial zone, are found to have the opposite behavior for the two types of susceptibility: marine stratocumulus are characterized by low values of absolute susceptibility and high values of relative susceptibility while the opposite is true for equatorial shallow cumulus. This behavior can be easily explained with the aid of Figure 5, which shows the geographical distribution of optical thickness, effective radius, liquid phase cloud fraction and ICA albedo of regions covered by liquid clouds for October. In marine stratocumulus regions, moderate optical thicknesses and small effective radii prevail yielding small absolute susceptibility and large relative susceptibility (see Figure 2 in Part 1); in marine convective regions small optical thicknesses and large effective radii prevail yielding large absolute susceptibility and small relative susceptibility. Because, however, in the former case the cloud fractions are much larger than in the latter (Figure 5, bottom left), a definitive assessment of the overall radiative impact requires a more detailed examination. It must be noted that the tendency of high absolute susceptibility marine regions to be also regions of low cloud fractions is rather general. This is because an anticorrelation exists between marine liquid cloud fraction and retrieved r_e (Figure 6). The anticorrelation is virtually nonexistent over land (correlation coefficient ~0.1 versus 0.5 over ocean). It remains unclear whether it reflects a real physical coupling or an artifact of the 1-D retrieval algorithm operating under broken cloudy conditions. Another feature that holds true for both absolute and relative susceptibility is the trend for lower values at high latitudes than at low latitudes (see also Figure 8). This is probably because of the simultaneous increase in both optical thickness and surface albedo, and with the liquid cloud fraction quite low in these regions (especially Antarctica), the radiative consequences are minimized even further.

[22] The frequency distributions of Terra absolute and relative susceptibility over land and ocean are depicted in Figures 7a and 7b, respectively. The aforementioned contrast between ocean and land values is apparent. The continental absolute susceptibility histograms are conspicuously narrower than their marine counterparts. This is less true for the relative susceptibility histograms, the shape of which depends more on ocean-land optical thickness con-

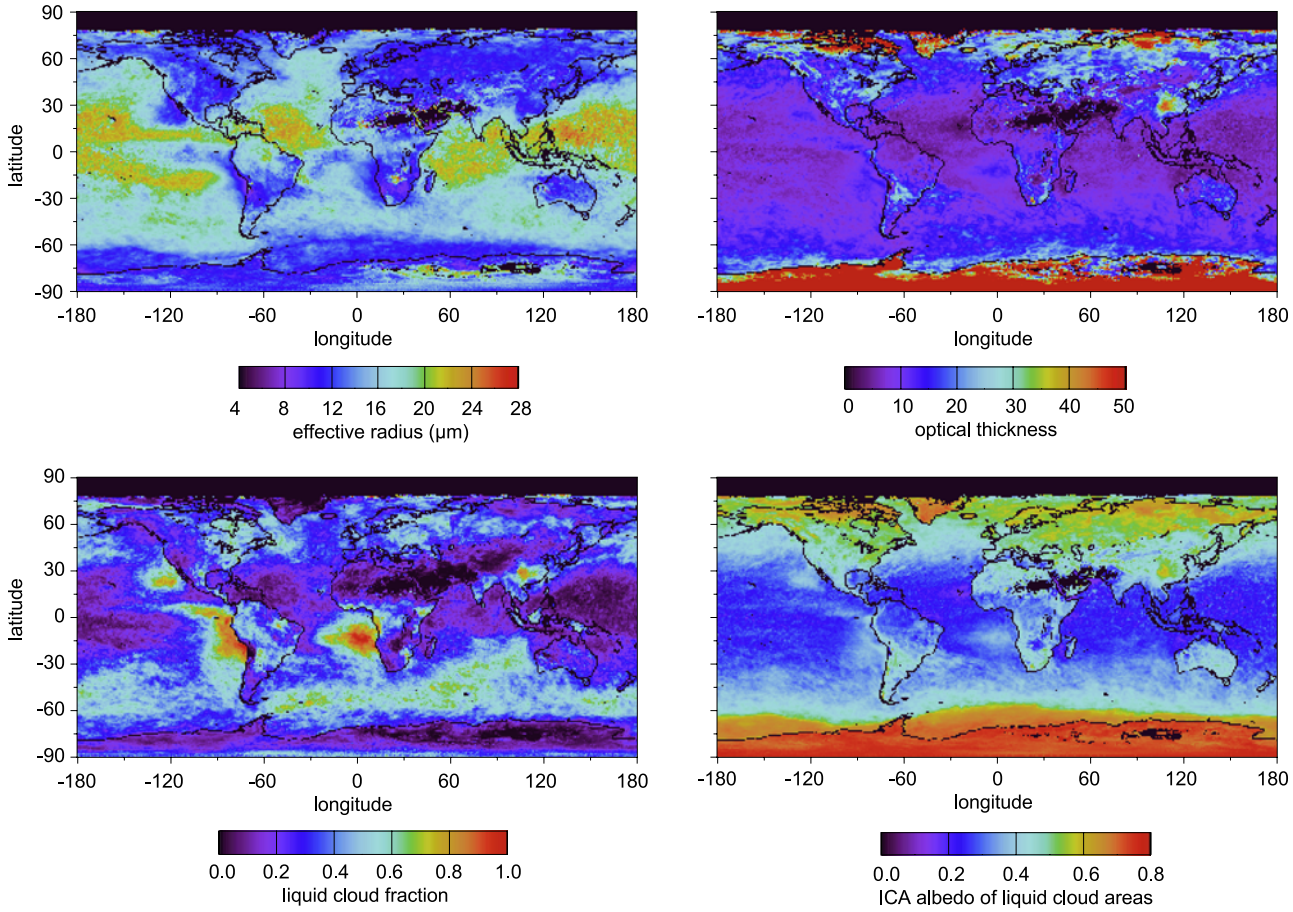

Figure 5. Monthly averages of liquid cloud effective radius, optical thickness, and cloud fraction, along with the ICA albedo of the portion of the grid point covered by liquid clouds for MODIS Terra October 2005.

trasts rather than effective radius contrasts. Prominent low value modes in the land histograms during January and October come from susceptibility calculations over Antarctica. The oceanic low-value peaks in April and July originate from the Arctic Ocean.

3.6. Terra Versus Aqua

[23] The zonal distribution of cloud fraction weighted absolute and relative susceptibility for Terra and Aqua are compared in Figures 8a and 8b for all 4 months analyzed in this study. Differences are quite small with only slight time-of-day (~3 h) differences evident in the tropics. Figure 9, however, which shows scatterplots of individual grid point data from January monthly averages, suggests that at smaller spatial scales the differences are more significant, albeit not systematic. Since there are no SZA differences between the symmetric (around local solar noon) morning and afternoon orbits, and since surface albedo and atmospheric condition changes are negligible, all the variability in Figure 9 is driven by temporal changes in cloud properties.

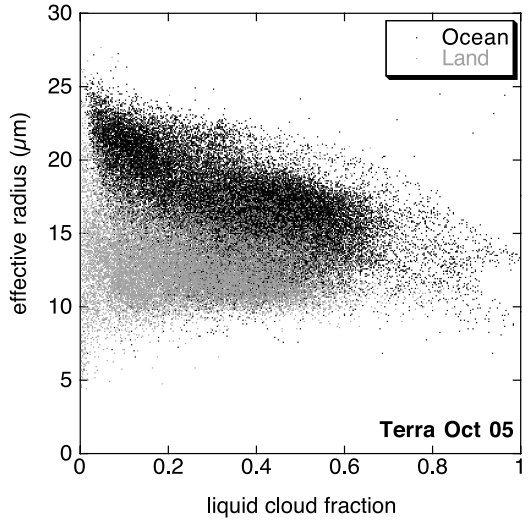

Figure 6. Relationship between monthly averaged grid point mean liquid cloud fraction and effective radius for oceanic and continental regions for MODIS Terra October 2005 data.

4. Global Susceptibility Forcing

[24] The albedo susceptibility estimates performed in this study become useful in a climatic context when translated into sensitivities in the global TOA reflected flux. In our

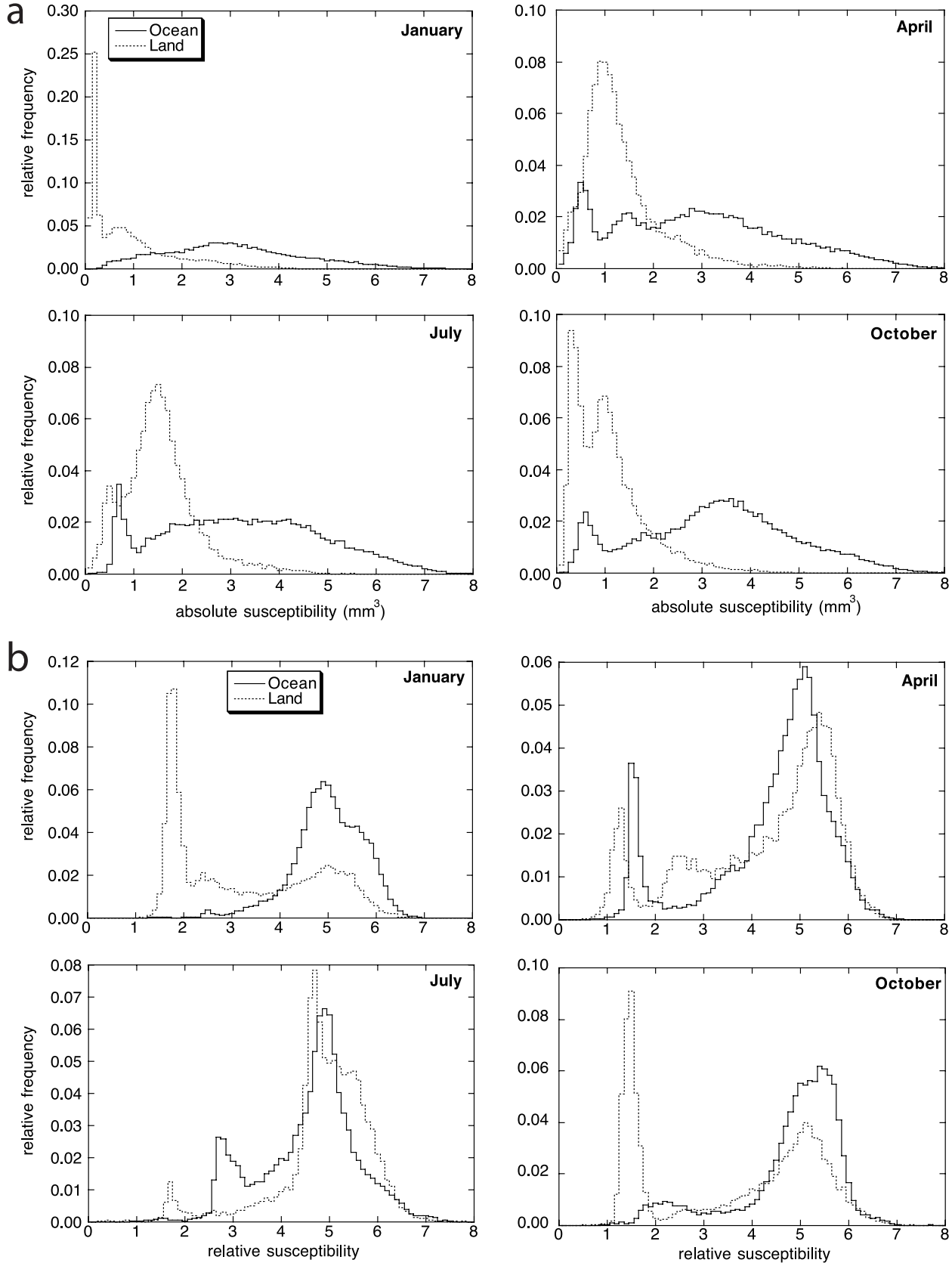

Figure 7. (a) Histograms of MODIS Terra monthly averaged ICA absolute susceptibility ($\Delta N = 1$ cm^{-3}, $w = 0.3$ gm^{-3}) from separate aggregation of oceanic and continental grid points for the 4 months examined in this study. (b) As in Figure 7a but for relative susceptibility $\times$ 1000 ($\Delta N/N = 10\%$).

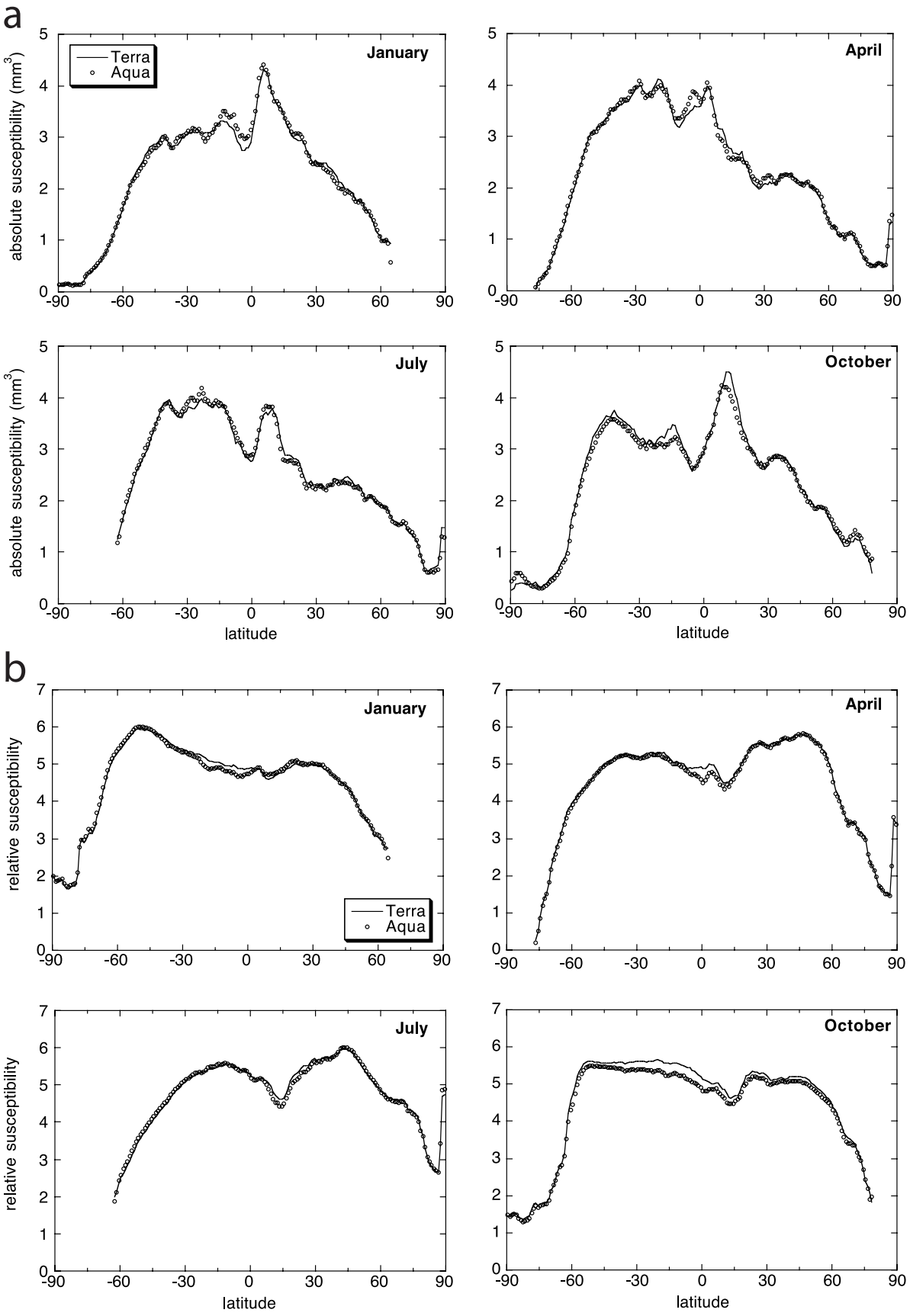

Figure 8. (a) Zonal comparisons of MODIS Terra and Aqua monthly averaged ICA absolute susceptibility ($\Delta N = 1$ cm^{-3}, $w = 0.3$ gm^{-3}) for the 4 months examined in this study. (b) As in Figure 8a but for relative susceptibility $\times$ 1000 ($\Delta N/N = 10\%$).

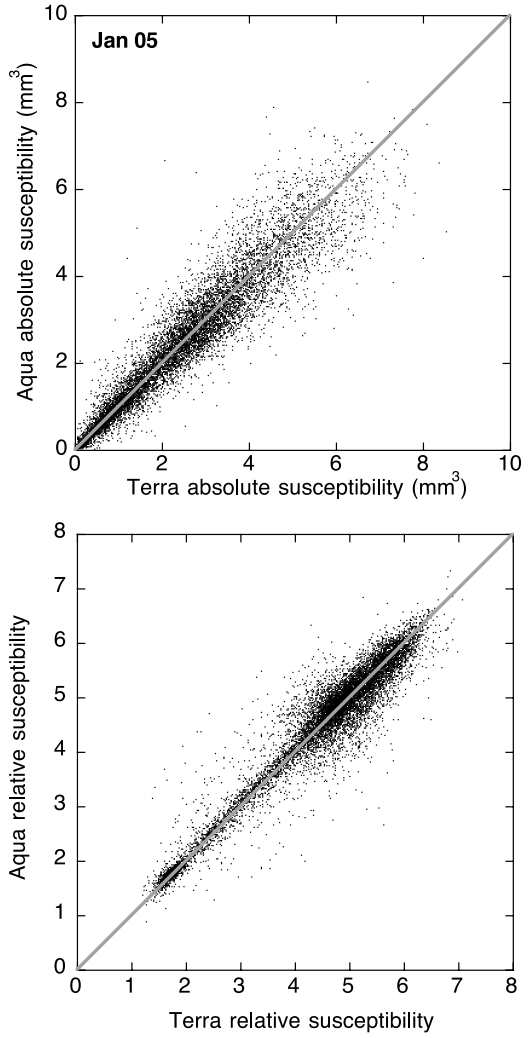

Figure 9. Scatterplot of Aqua versus Terra monthly averaged grid point (top) absolute (ΔN = 1 cm^{-3}, w = 0.3 gm^{-3}) and (bottom) relative ($\Delta N/N$ = 10%) ICA susceptibilities for January 2005. Relative susceptibilities have been multiplied by 1000. Every 5th grid point is plotted.

study, this "global susceptibility forcing" corresponds to a global Indirect Aerosol Forcing (IAF) of the 1st type (constant liquid water) for uniform absolute CDNC perturbations of 1 cm^{-3} (with water content w = 0.3 g m^{-3}) or relative perturbations of 10% due to an above-background infusion of CCNs. A summary of this global susceptibility forcing, calculated from the product of the reflected TOA flux perturbation and liquid cloud fraction for each grid point and appropriate areal weighting, is provided in Figure 10. The Level 3 SZA data were used in these calculations and therefore do not reflect a true diurnal average. For our chosen globally uniform CDNC perturbations and reference values of w and k (for absolute susceptibility only), the susceptibility forcing ranges from ~0.8–1.8 W m^{-2} which is similar to that from other IAF studies (e.g., review of *Lohmann and Feichter* [2005] and *Intergovernmental Panel on Climate Change* [2007, Figure 2.14]). While our global values are not strictly comparable to modeling results on postindustrial (i.e., past) IAF, they nevertheless demonstrate that for reasonable assumptions about CDNC perturbations, current liquid clouds will produce future IAFs of the same order as estimated past perturbations. The ~1 W m^{-2} range in the values we obtain can be traced back to the month of the year (maximum in October, minimum in April), the time of the day (morning forcing consistently larger than afternoon forcing), and most importantly, the type of susceptibility: for typical clouds, 10% relative CDNC perturbations yield larger effective radius perturbations than 1 cm^{-3} absolute perturbations and thus larger IAFs. Another major factor that makes relative susceptibility forcing larger than absolute susceptibility forcing is the pairing of the former with higher values of cloud fraction. In other words, the largest absolute susceptibilities are not as climatically important since they are coupled with smaller cloud fractions.

5. Summary and Discussion

[25] The albedo susceptibility for regions covered by unobscured liquid clouds, i.e., the sensitivity of TOA albedo to perturbations in cloud droplet number concentration (CDNC) was calculated on global scales using the expanded susceptibility definitions and methodologies presented in our companion Part 1 paper. The calculations extend pre-

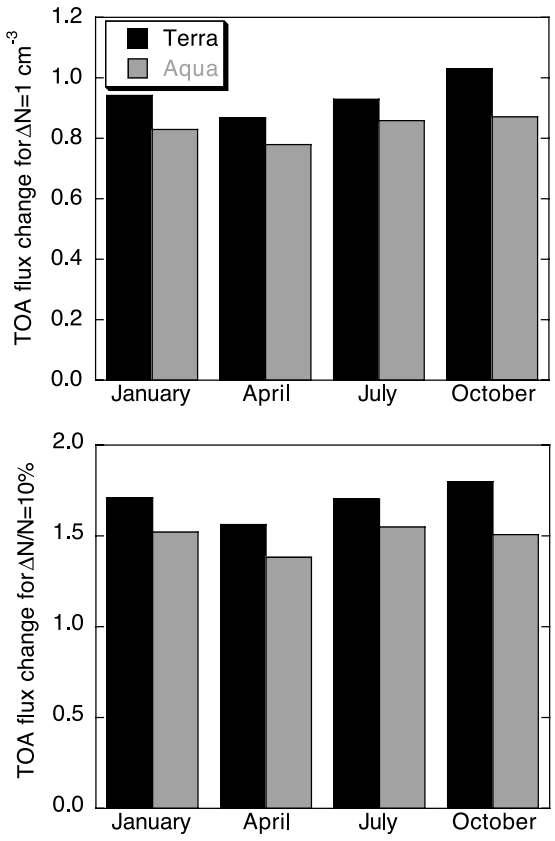

Figure 10. (top) Top-of-atmosphere global ICA reflected flux perturbation for all months and both MODIS (Terra and Aqua) retrieved cloud distributions, for a uniform ΔN = 1 cm^{-3} CDNC perturbation assuming w = 0.3 gm^{-3} for all liquid clouds. (bottom) As in Figure 10 (top) but for a uniform $\Delta N/N$ = 10% perturbation.

vious susceptibility estimates by including relative CDNC changes, perturbations in cloud droplet asymmetry parameter and single-scattering albedo, atmospheric/surface effects, and by covering the full range of the solar spectrum. The cloud properties (optical thickness, effective radius) used as input in the susceptibility calculations come from recent MODIS Terra and Aqua Collection 5 gridded ($1^\circ \times 1^\circ$) data for January, April, July and October of 2005.

[26] The geographical distribution of susceptibility corresponding to differential absolute (''absolute susceptibility'') as well as relative (''relative susceptibility'') CDNC changes is markedly different and demonstrates that the detailed nature of the cloud microphysical perturbation is important in determining the radiative forcing response of the first indirect effect. The differences can be explained by the different dependencies of absolute and relative susceptibility to the unperturbed cloud properties. Given some apparent anticorrelation between marine cloud fraction and effective radius, large absolute susceptibilities over ocean often pair with low values of cloud fraction, thus reducing the radiative importance of many high susceptibility clouds. Both types of susceptibility exhibit common features such as the tendency to decrease with latitude, to be higher over ocean than over land and to be statistically similar between the morning and afternoon MODIS overpasses.

[27] Our absolute susceptibility calculations assume a liquid water content of 0.3 gm^{-3}. The assumption of a specific value of liquid water content cannot be circumvented unless the CDNC or geometrical cloud thickness is prescribed. While absolute susceptibilities for different values of liquid water content can be obtained by simply rescaling calculations that used our reference value of 0.3 g m^{-3}, applying the assumption of a globally invariant liquid water content introduces a significant amount of uncertainty in the susceptibility calculations. Nevertheless, if distributions of water content were to become available, absolute susceptibilities could be reestimated without new radiative transfer calculations. Relative CDNC perturbations avoid the restriction of knowing or assuming liquid water content, and the corresponding cloud albedo perturbation is also accurately scalable with respect to $\Delta N/N$ (see Part 1); but even in this case spatial distributions of $\Delta N/N$ are needed for accurate susceptibility forcing calculations. Addressing spatial variability of perturbations will require ancillary data sets from global models with realistic and validated microphysical parameterizations.

[28] Still, the current susceptibility calculations can help improve the understanding of the Indirect Aerosol Effect (IAE) of liquid clouds in several ways: obtaining a range of sensible assessments of the 1st IAE global radiative forcing (our realistic, but moderate uniform CDNC perturbations yield forcings on the order of 1–2 W m^{-2}); identifying the regions of the globe that are more prone to significant IAE radiative perturbations not only because of their proximity to pollution sources, but also because of the nature of the prevailing cloud properties under current climate conditions; delineating the limits of IAE predictability with MODIS-like passive retrievals of cloud and aerosol properties; and assessing the ability of GCMs to simulate both global and regional radiative perturbations due to IAE. In particular, with respect to global modeling, the susceptibility study presented here is intended to improve the understanding of how well current cloud properties need to be known to obtain reasonably accurate estimates of cloud radiative forcing sensitivities. This in turn will provide guidance on the accuracy needed by explicit cloud microphysical schemes in GCMs in order for model cloud distributions to reproduce realistic values of current-day susceptibilities. Continued progress in examining the consequences of satellite-derived cloud climatologies on cloud-related radiative forcing sensitivities is critical for understanding the IAE and a variety of other cloud-related climate change issues.

[29] **Acknowledgments.** We are grateful for the many years of contributions from the MODIS instrument and science teams. Both authors wish to acknowledge support from the NASA Radiation Science Program. L. Oreopoulos also gratefully acknowledges support from the U.S. Department of Energy, Office of Science, Office of Biological and Environmental Research, Environmental Sciences Division as part of the ARM program under grant DE-FG02-07ER64354.

References

Barker, H. W. (2000), Indirect aerosol forcing by homogenous and inhomogeneous clouds, *J. Clim.*, *13*, 4042–4049, doi:10.1175/1520-0442(2000)013<4042:IAFBHA>2.0.CO;2.

Bohren, C. F. (1987), Multiple scattering of light and some of its observable consequences, *Am. J. Phys.*, *55*, 524–533, doi:10.1119/1.15109.

Bréon, F.-M., D. Tanré, and S. Generoso (2002), Aerosol effect on cloud droplet size monitored from satellite, *Science*, *295*, 834–838, doi:10.1126/science.1066434.

Cahalan, R. F., W. Ridgway, W. J. Wiscombe, T. L. Bell, and J. B. Snider (1994), The albedo of fractal stratocumulus clouds, *J. Atmos. Sci.*, *51*, 2434–2455, doi:10.1175/1520-0469(1994)051<2434:TAOFSC>2.0.CO;2.

Chin, M., T. Diehl, P. Ginoux, and W. Malm (2007), Intercontinental transport of pollution and dust aerosols: Implications for regional air quality, *Atmos. Chem. Phys.*, *7*, 5501–5517.

Chou, M.-D., and M. J. Suarez (2002), A solar radiation parameterization for atmospheric studies, *NASA Tech. Memo.*, *NASA/TM-1999-10460*, vol. 15, 52 pp.

Chou, M.-D., M. J. Suarez, C.-H. Ho, M. M.-H. Yan, and K.-T. Lee (1998), Parameterizations for cloud overlapping and shortwave single-scattering properties for use in general circulation and cloud ensemble models, *J. Clim.*, *11*, 202–214, doi:10.1175/1520-0442(1998)011<0202:PFCOAS>2.0.CO;2.

Chuang, C. C., J. E. Penner, J. M. Prospero, K. E. Grant, G. H. Rau, and K. Kawamoto (2002), Cloud susceptibility and the first aerosol indirect forcing: Sensitivity to black carbon and aerosol concentrations, *J. Geophys. Res.*, *107*(D21), 4564, doi:10.1029/2000JD000215.

Coakley, J. A., Jr., and C. D. Walsh (2002), Limits to the aerosol indirect radiative forcing derived from observations of ship tracks, *J. Atmos. Sci.*, *59*, 668–680, doi:10.1175/1520-0469(2002)059<0668:LTTAIR>2.0.CO;2.

Derber, J. C., D. F. Parrish, and S. J. Lord (1991), The new global operational analysis system at the National Meteorological Center, *Weather Forecast.*, *6*, 538–547, doi:10.1175/1520-0434(1991)006<0538:TNGOAS>2.0.CO;2.

Fountoukis, C., and A. Nenes (2005), Continued development of a cloud droplet formation parameterization for global climate models, *J. Geophys. Res.*, *110*, D11212, doi:10.1029/2004JD005591.

Holben, B. N., et al. (1998), AERONET—A federated instrument network and data archive for aerosol characterization, *Remote Sens. Environ.*, *66*, 1–16, doi:10.1016/S0034-4257(98)00031-5.

Intergovernmental Panel on Climate Change (2007), *Climate Change 2007: The Physical Science Basis*, edited by S. Solomon, D. Qin, and M. Manning, Geneva, Switzerland. (Available at http://ipcc-wg1.ucar.edu/wg1/wg1-report.html)

Kaufman, Y. J., I. Koren, L. A. Remer, D. Rosenfeld, and Y. Rudich (2005), The effect of smoke, dust, and pollution aerosol on shallow cloud development over the Atlantic Ocean, *Proc. Natl. Acad. Sci. U. S. A.*, *102*, 11,207–11,212, doi:10.1073/pnas.0505191102.

King, M. D., W. P. Menzel, Y. J. Kaufman, D. Tanre, B.-C. Gao, S. Platnick, S. A. Ackerman, L. A. Remer, R. Pincus, and P. A. Hubanks (2003), Cloud and aerosol properties, precipitable water, and profiles of temperature and humidity, *IEEE Trans. Geosci. Remote Sens.*, *41*, 442–458, doi:10.1109/TGRS.2002.808226.

Koren, I., Y. J. Kaufman, D. Rosenfeld, L. A. Remer, and Y. Rudich (2005), Aerosol invigoration and restructuring of Atlantic convective clouds, *Geophys. Res. Lett.*, *32*, L14828, doi:10.1029/2005GL023187.

Lohmann, U., and J. Feichter (2005), Global indirect aerosol effects: A review, *Atmos. Chem. Phys.*, *5*, 715–737.

Martin, G. M., D. W. Johnson, and A. Spice (1994), The measurement and parameterization of effective radius of droplets in warm stratocumulus clouds, *J. Atmos. Sci.*, *51*, 1823–1842, doi:10.1175/1520-0469(1994)051<1823:TMAPOE>2.0.CO;2.

Ming, Y., V. Ramaswamy, L. J. Donner, and V. T. J. Phillips (2006), A new parameterization of cloud droplet activation applicable to general circulation models, *J. Atmos. Sci.*, *63*, 1348–1356, doi:10.1175/JAS3686.1.

Moody, E. G., M. D. King, S. Platnick, C. B. Schaaf, and F. Gao (2005), Spatially complete global spectral surface albedos: Value-added datasets derived from Terra MODIS land products, *IEEE Trans. Geosci. Remote Sens.*, *43*, 144–158, doi:10.1109/TGRS.2004.838359.

Oreopoulos, L., R. F. Cahalan, and S. Platnick (2007), The plane-parallel albedo bias of liquid clouds from MODIS observations, *J. Clim.*, *20*, 5114–5125, doi:10.1175/JCLI4305.1.

Platnick, S., and L. Oreopoulos (2008), Radiative susceptibility of cloudy atmospheres to droplet number perturbations: 1. Theoretical analysis and examples from MODIS, *J. Geophys. Res.*, *113*, D14S20, doi:10.1029/2007JD009654.

Platnick, S., and S. Twomey (1994), Determining the susceptibility of cloud albedo to changes in droplet concentration with the Advanced Very High Resolution Radiometer, *J. Appl. Meteorol.*, *33*, 334–347, doi:10.1175/1520-0450(1994)033<0334:DTSOCA>2.0.CO;2.

Platnick, S., M. D. King, S. A. Ackerman, W. P. Menzel, B. A. Baum, J. C. Riedi, and R. A. Frey (2003), The MODIS cloud products: Algorithms and examples from Terra, *IEEE Trans. Geosci. Remote Sens.*, *41*, 459–473, doi:10.1109/TGRS.2002.808301.

Sekiguchi, M., T. Nakajima, K. Suzuki, K. Kawamoto, A. Higurashi, D. Rosenfeld, I. Sano, and S. Mukai (2003), A study of the direct and indirect effects of aerosols using global satellite data sets of aerosol and cloud parameters, *J. Geophys. Res.*, *108*(D22), 4699, doi:10.1029/2002JD003359.

L. Oreopoulos, Joint Center for Earth Systems Technology, University of Maryland, Baltimore County, Baltimore, MD 21228, USA.

S. Platnick, Laboratory for Atmospheres, NASA Goddard Space Flight Center, Greenbelt, MD 20771, USA. (steven.platnick@nasa.gov)